

# Fluid Simulations of Three-Dimensional Reconnection that Capture the Lower-Hybrid Drift Instability

F. Allmann-Rahn<sup>1†</sup>, S. Lautenbach<sup>1</sup>, R. Grauer<sup>1</sup>, and R. D. Sydora<sup>2</sup>

<sup>1</sup>Institute for Theoretical Physics I, Ruhr University Bochum, Germany

<sup>2</sup>Department of Physics, University of Alberta, Edmonton, Alberta T6G 2E1, Canada

Fluid models that approximate kinetic effects have received attention recently in the modelling of large scale plasmas such as planetary magnetospheres. Where fully kinetic computations are not an option, fluid or hybrid models can be an excellent replacement. In three-dimensional reconnection, however, both reconnection itself and current sheet instabilities need to be represented appropriately, which has been an issue before. We show that a heat flux closure based on pressure gradients enables a ten moment fluid model to capture the lower-hybrid drift instability within a reconnection simulation. Characteristics of the instability are examined with fluid and kinetic continuum models, and its role in the three-dimensional reconnection simulation is analysed. It is found that the initial perturbation level has significant impact on the resulting turbulence.

## 1. Introduction

The reconnection of magnetic field lines in a plasma causes release of magnetic energy. Magnetic reconnection takes place, for example, in solar flares and the Earth's magnetosphere and thus influences space weather. On the other hand it also occurs in fusion devices where it can induce further instabilities and affect confinement of the fusion plasma.

In the last decades, reconnection has been the subject of many numerical studies, especially starting with the GEM challenge (Birn *et al.* 2001) where a widely used setup for reconnection simulations was defined. The deeper understanding of fast reconnection gained through numerical simulations has been complemented by laboratory experiments such as the Magnetic Reconnection Experiment (MRX) (Yamada *et al.* 1997). In 2015 NASA started the Magnetospheric Multiscale Mission (MMS) which was the first spacecraft to directly measure reconnection in the magnetosphere.

The increase in computational power and the availability of data from MMS measurements open up new possibilities and define the directions of current reconnection research. We will briefly list what we consider to be central research subjects. One important point is of course the interpretation of MMS measurements, and numerical simulations are a valuable tool in this regard. On the other hand, the MMS measurements can also be used to validate the numerical models. Recent studies showed agreement with MMS data for kinetic particle-in-cell (PIC) simulations (e.g. Nakamura *et al.* (2018a)) and for ten-moment fluid simulations (TenBarge *et al.* 2019). Both models retain the anisotropic pressure tensor which is one mechanism to break the frozen-in condition in collisionless reconnection (Egedal *et al.* 2019). Generally, there is hope for more insights from the

† Email address for correspondence: far@tp1.rub.de

MMS mission concerning dissipation processes (e.g. Landau damping) that break the frozen-in law.

Another question is that of three-dimensionality. Due to limited computational resources, past research focused on two-dimensional reconnection where the third dimension is assumed to be homogeneous. Under which conditions this is a good approximation and how much influence current sheet instabilities and resulting turbulence have, is still a largely open question. Relevant instabilities are for example the lower-hybrid drift instability (LHDI) and the firehose instability (Le *et al.* 2019) as well as the current sheet shear instability (CSSI) and Kelvin-Helmholtz/kink type instabilities (Fujimoto & Sydora 2012, 2017).

The LHDI, which is the main subject of this work, has been extensively studied theoretically and in kinetic simulations (e.g. Daughton 2003) along with frequent measurements of LHDI fluctuations being made at magnetospheric reconnection sites, such as the magnetopause, and in laboratory reconnection experiments. The free energy source for the instability are inhomogeneities in the magnetic field and plasma pressure which drive the relative drifts of electrons and ions. Even though the LHDI does not significantly alter the reconnection rate it does lead to enhanced anomalous plasma transport which relaxes gradients, for instance the density, which in turn can give rise to secondary instabilities such as the CSSI that is driven by the electron flow shear (Fujimoto & Sydora 2017). Kelvin-Helmholtz type instabilities are also induced by the LHDI and lead to kinking of the current sheet (Lapenta *et al.* 2003).

Finally, the impact of reconnection on macroscopic systems like planetary magnetospheres is of great interest. Generally, being able to simulate large scale, global systems with models more accurate than MHD brings new opportunities: both for getting a better understanding of physical processes in the magnetosphere and for the application in space weather forecast. Treating global systems with fully kinetic particle-in-cell (PIC) models is difficult due to their high computational expense. Therefore, recent studies utilised ten-moment fluid models with good success. Wang *et al.* (2018) modelled the magnetosphere of the Jupiter moon Ganymede, and Dong *et al.* (2019) studied the interaction between the solar wind and Mercury’s magnetosphere. The applicability of multi-fluid models for very large scales also profits from their ability to under-resolve scales and still yield appropriate results (Wang *et al.* 2020). However, the ten-moment model used in aforementioned studies (first presented in Wang *et al.* (2015)) has some drawbacks, indicating that the approximation of kinetic effects in the model needs to be improved.

Different directions can be taken concerning the integration of kinetic effects in fluid models, and we want to highlight some of them. Kinetic effects include non-collisional damping mechanisms such as Landau damping. A very successful fluid model that approximates Landau damping in one dimension using calculations in Fourier space was introduced by Hammett & Perkins (1990) and Hammett *et al.* (1992). It was later extended (see e.g. Snyder *et al.* (1997) and Passot & Sulem (2003)) and is still relevant today for one-dimensional cases and as a basis for other closures.

In two and three dimensions, it is a reasonable assumption that damping mechanisms will drive temperature to a more isotropic state. Fluid models that include a term which drives the pressure tensor to isotropy were applied in collisionless reconnection by Hesse *et al.* (1995) and Johnson & Rossmannith (2010). Later, a connection was made between the Landau damping fluid closures and pressure isotropisation by Wang *et al.* (2015). The result was the fluid model that was used for the mentioned simulations of Ganymede’s and Mercury’s magnetospheres. However, some problems became apparent; using this heat flux closure in island coalescence reconnection, one does not obtain the same reconnection

rate scaling with system size that is present in kinetic simulations (Ng *et al.* 2015). It was also found that the simple isotropisation closure does not support the LHDI when its free parameter is chosen as in reconnection simulations. Both issues can be addressed to some degree with a closure expression that, like the original Hammett-Perkins approach, incorporates calculations in Fourier space (Ng *et al.* 2017, 2019). Such a non-local closure, however, is not suitable for large scale simulations because Fourier transforms and the necessary integration along field lines are computationally extensive (Ng *et al.* 2019).

A heat flux closure that is based on temperature gradients was proposed by Sharma *et al.* (2003, 2006). It performed well in simulations of the magnetorotational instability and is also related to Landau fluid closures. Besides Landau damping, particle trapping is another relevant kinetic effect in collisionless reconnection. A fluid model that includes particle trapping mechanisms was developed by Le *et al.* (2009) with an extension of the classic equations of state. This closure yields good results in guide field reconnection (also see Egedal *et al.* (2013); Le *et al.* (2016)) but is not applicable in systems without guide field. In its current form, the model also does not support the LHDI (Le *et al.* 2019).

In this paper, we simulate three-dimensional reconnection and current sheet instabilities using the heat flux closure introduced in Allmann-Rahn *et al.* (2018). There, heat flux is assumed to be proportional to the gradient of the pressure tensor's deviation from isotropy. Thus, both the isotropisation character of the closely related closure in Wang *et al.* (2015) and the gradient dependence of the classic Landau fluid closures are retained.

## 2. Physical Models and Numerics

A plasma is accurately described by distribution functions  $f_s(\mathbf{x}, \mathbf{v}, t)$  for each species  $s$ . The amount of particles located between  $\mathbf{x}$  and  $\mathbf{x} + d\mathbf{x}$  with velocities between  $\mathbf{v}$  and  $\mathbf{v} + d\mathbf{v}$  is then given by  $f_s(\mathbf{x}, \mathbf{v}, t) d\mathbf{x} d\mathbf{v}$ . For collisionless plasmas, the Vlasov equation determines the evolution of the distribution functions:

$$\frac{\partial f_s}{\partial t} + \mathbf{v} \cdot \nabla f_s + \frac{q_s}{m_s} (\mathbf{E} + \mathbf{v} \times \mathbf{B}) \cdot \nabla_v f_s = 0. \quad (2.1)$$

Various physical quantities can be obtained from the distribution function by taking moments. Multiplying by powers of  $\mathbf{v}$  and integrating over velocity space leads to expressions for particle density  $n_s(\mathbf{x}, t) = \int f_s(\mathbf{x}, \mathbf{v}, t) d\mathbf{v}$ , mean velocity  $\mathbf{u}_s(\mathbf{x}, t) = \frac{1}{n_s(\mathbf{x}, t)} \int \mathbf{v} f_s(\mathbf{x}, \mathbf{v}, t) d\mathbf{v}$ , pressure  $P_s = m_s \int \mathbf{v}' \otimes \mathbf{v}' f_s d\mathbf{v}$  and heat flux  $\mathbf{Q}_s = m_s \int \mathbf{v}' \otimes \mathbf{v}' \otimes \mathbf{v}' f_s d\mathbf{v}$ . Here,  $\otimes$  is the tensor product and  $\mathbf{v}' = \mathbf{v} - \mathbf{u}$ .

The plasma quantities evolve according to the so called multi-fluid equations. These can be derived by taking moments of the Vlasov equation and making a physical assumption in order to close the resulting hierarchy. If moments up to the pressure tensor are considered, the ten moment equations follow (named like that because ten equations need to be solved):

$$\frac{\partial n_s}{\partial t} + \nabla \cdot (n_s \mathbf{u}_s) = 0, \quad (2.2)$$

$$m_s \frac{\partial (n_s \mathbf{u}_s)}{\partial t} = n_s q_s (\mathbf{E} + \mathbf{u}_s \times \mathbf{B}) - \nabla \cdot \mathcal{P}_s, \quad (2.3)$$

$$\frac{\partial \mathcal{P}_{ij}^s}{\partial t} - q_s (n_s u_{[i}^s E_{j]} + \frac{1}{m_s} \epsilon_{[ikl} \mathcal{P}_{kj]}^s B_l) = -(\nabla \cdot \mathcal{Q}_s)_{ij}. \quad (2.4)$$

$\mathcal{P}_s = m_s \int \mathbf{v} \otimes \mathbf{v} f_s d\mathbf{v}$  and  $\mathcal{Q}_s = m_s \int \mathbf{v} \otimes \mathbf{v} \otimes \mathbf{v} f_s d\mathbf{v}$  are the second and third moment

of the distribution function (multiplied by mass),  $\epsilon_{ikl}$  is the Levi-Civita symbol and the square brackets denote the sum over as many permutations of indices as needed to make the tensors symmetric, for example

$$u_{[i}E_{j]} = u_iE_j + u_jE_i.$$

This set of equations needs a closure approximation for the divergence of the heat flux which is discussed in Sec. 3. Heat flux  $\mathbf{Q}$  is related to the distribution function's moments according to  $Q_{ijk} = \mathcal{Q}_{ijk} - u_{[i}\mathcal{P}_{jk]} + 2mn u_i u_j u_k$ .

The ten moment equations reduce to five moment equations, if the temperature (and pressure, respectively) is isotropic. Then Eq. (2.3) becomes

$$m_s \frac{\partial(n_s \mathbf{u}_s)}{\partial t} = n_s q_s (\mathbf{E} + \mathbf{u}_s \times \mathbf{B}) - \frac{1}{3} \nabla (2\mathcal{E}_s - m_s n_s u_s^2) - \nabla \cdot (m_s n_s \mathbf{u}_s \otimes \mathbf{u}_s), \quad (2.5)$$

with scalar energy density  $\mathcal{E}_s = \frac{m_s}{2} \int v^2 f_s d\mathbf{v}$ . Additionally assuming zero heat flux in this isotropic limit, Eq. (2.4) becomes

$$\frac{\partial \mathcal{E}_s}{\partial t} + \frac{1}{3} \nabla \cdot (\mathbf{u}_s (5\mathcal{E}_s - m_s n_s u_s^2)) - q_s n_s \mathbf{u}_s \cdot \mathbf{E}_s = 0. \quad (2.6)$$

Physical units in the simulations are normalised as follows: Length is normalised over ion inertial length  $d_{i,0}$  based on density  $n_0$ , velocity over ion Alfvén velocity  $v_{A,0}$  based on the magnetic field  $B_0$ , time over the inverse of the ion cyclotron frequency  $\Omega_{i,0}^{-1}$  and mass over ion mass  $m_i$ . Further normalisations are vacuum permeability  $\mu_0 = 1$  and Boltzmann constant  $k_B = 1$ .

The Vlasov simulations in this paper use the positive and flux-conservative (PFC) method by Filbet *et al.* (2001), which is a semi-Lagrangian method, combined with back-substitution (Schmitz & Grauer 2006) for the velocity updates. For the fluid equations we employ a centrally weighted essentially non-oscillating (CWENO) method (Kurganov & Levy 2000) and the third-order Runge-Kutta scheme by Shu & Osher (1988). Maxwell's equations are solved by means of the finite-difference time-domain (FDTD) method.

All of the simulations were performed using the GPU accelerated *muphy2* multi-physics simulation code developed at Institute for Theoretical Physics I, Ruhr University Bochum. The code is designed for running kinetic, fluid and hybrid schemes either individually or spatially coupled to each other.

### 3. Gradient-Driven Heat Flux Closure

A heat flux term that models kinetic dissipation mechanisms needs to introduce damping into the ten moment equations. This can be achieved, for example, with an expression that takes the form of Fourier's law

$$\mathbf{q} = -n D \nabla T \quad (3.1)$$

with heat flux vector  $\mathbf{q}$  and thermal conductivity  $D$ . Heat flux approximations based on temperature gradients have been used for plasmas in the classic Braginskii equations already (Braginskii 1965) and can also be the basis of Landau fluid closures. Hammett & Perkins (1990) and Hammett *et al.* (1992) used phase mixing theory to obtain in one-dimensional Fourier space

$$\tilde{q} = -n_0 \chi_1 \sqrt{2} \frac{v_t}{|k|} i k \tilde{T} \quad (3.2)$$

where tildes denote perturbed quantities and the conductivity  $D = \chi_1 \sqrt{2} \frac{v_t}{|k|}$  is dependent on the wave number  $k$  and thermal velocity  $v_t$ . This closure is suitable for approximating kinetic Landau damping.

Fourier's law is trivially generalised to three dimensions by replacing the heat flux vector with the third order heat flux tensor  $\mathbf{Q}$  and the scalar temperature with the second order temperature tensor  $\mathbf{T}$ . Then the gradient of the temperature tensor yields a third order tensor. The conductivity from the Landau fluid closure can also easily be transferred as it contains only the absolute value of the wave number. To avoid calculations in Fourier space, Wang *et al.* (2015) introduced a simplification where the continuous wave number field is replaced by a single typical wave number  $\mathbf{k}_0$ , and we follow this approach. Landau damping is the kinetic damping of plasma oscillations, thus  $1/|\mathbf{k}_{s,0}| = d_{s,0}$  is a natural choice,  $d_{s,0}$  being the species inertial length based on  $n_0$ . We choose an initial ansatz  $\mathbf{q} = -D \nabla P$  slightly different from Fourier's law which originates from comparisons with kinetic simulations. Since Landau damping is modelled, damping is supposed to act on fast changing gradients due to wave-like plasma activities and not on gradients from slowly changing background quantities. Therefore, we subtract an equilibrium pressure which is comparable to the consideration of perturbed quantities like in the Hammett-Perkins closure. For species  $s$ , the resulting heat flux then has the form

$$\mathbf{Q}_s = -\frac{\chi}{k_{s,0}} v_{t,s} \nabla (P_s - P_{s,0}) \quad (3.3)$$

with the dimensionless parameter  $\chi$  and an equilibrium pressure  $P_{s,0}$ . A Maxwell distribution is an equilibrium distribution at which no Landau damping occurs and the related pressure would then be isotropic. This motivation is in accordance with studies where a closure term that drives pressure towards isotropy led to good results (Hesse *et al.* 1995; Johnson & Rossmannith 2010; Wang *et al.* 2015). Since we need an approximation of  $\nabla \cdot \mathbf{Q}$  as a closure to the ten moment equations (cf. Eq. (2.4)), we take the divergence. The derivative of  $v_{t,s}$  is assumed to be small and is neglected, and we obtain the Laplacian of the pressure tensor which is simply the Laplacian applied to each of its components. Then the final expression (hereafter called the gradient closure) is

$$\nabla \cdot \mathbf{Q}_s = -\frac{\chi}{k_{s,0}} v_{t,s} \nabla^2 (P_s - p_s \text{id}) \quad (3.4)$$

with  $\chi = 3$  and  $k_{s,0} = 1/d_{s,0}$ . The isotropic pressure is given by  $p_s = (P_{s,xx} + P_{s,yy} + P_{s,zz})/3$  and  $\text{id}$  denotes the identity matrix. The thermal velocity is defined as  $v_{t,s} = \sqrt{k_B T_s / m_s}$ . We find that  $\chi = 3$  is a reasonable value in a broad range of plasma configurations, but modifications to this dimensionless parameter can be made for further improving the agreement with kinetic calculations in specialised scenarios. Eq. (3.4) reduces to the isotropisation closure in Wang *et al.* (2015) with the approximation  $\nabla^2 \approx k_0^2$ . The gradient closure was first used in Allmann-Rahn *et al.* (2018).

For numerical stability and in order to enforce positive temperatures, we set a floor for the diagonal elements of the pressure tensor. The Laplacian is evaluated using second order central finite differences. This explicit method may need smaller time steps than the solution of the fluid equations themselves. Therefore, the computation of the closure is subcycled with a boundary exchange of the pressure tensor in between each subcycle. The amount of subcycles necessary depends on the cell size and the plasma configuration. In the three-dimensional reconnection simulation in this paper, for example, eight subcycles were used.

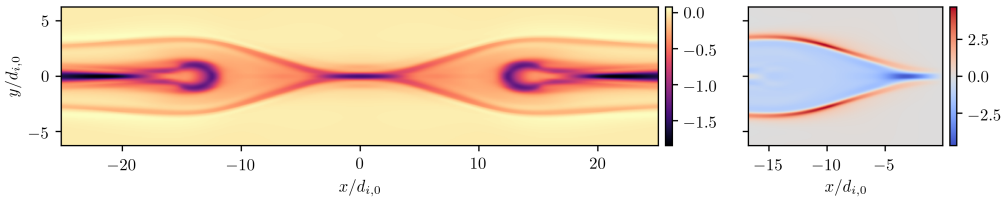


Figure 1: Current and velocity profiles in two-dimensional reconnection. Out-of-plane current  $j_z/(n_0 v_{A,0})$  (left) and electron outflow velocity  $u_{x,e}/v_{A,0}$  (right) at  $t = 65 \Omega_{i,0}^{-1}$ .

## 4. Two-Dimensional Reconnection

### 4.1. Harris Sheet

Magnetic reconnection can develop from a perturbation of the Harris sheet (Harris 1962) equilibrium. As initial conditions for the simulation we use parameters similar to the GEM (Geospace Environmental Modeling) reconnection setup (Birn *et al.* 2001) but with a larger domain of size  $L_x \times L_y = (32\pi \times 8\pi) d_{i,0} \approx (100 \times 25) d_{i,0}$ , resolved by  $2400 \times 600$  cells. Further differences are in the ion to electron mass ratio which is set to  $m_i/m_e = 100$  and in the speed of light  $c = 30 v_{A,0}$ . The domain is periodic in  $x$ -direction, has conducting walls for fields and reflecting walls for particles in  $y$ -direction and is translationally symmetric in  $z$ -direction. The initial configuration of the magnetic field is  $B_x(y) = B_0 \tanh(y/\lambda)$  and the particle density is  $n(y) = n_0 \text{sech}^2(y/\lambda) + n_b$  with  $\lambda = 0.5 d_{i,0}$  and background density  $n_b = 0.2 n_0$ . Temperature is defined by  $n_0 k_B (T_e + T_i) = B_0^2/(2\mu_0)$ ,  $T_i/T_e = 5$ . A perturbation of the magnetic field is added to break the equilibrium which takes the form  $\mathbf{B} = \hat{\mathbf{z}} \times \nabla \psi$  where the perturbation in the magnetic flux is given by  $\psi(x, y) = 0.1 \cos(2\pi x/L_x) \cos(\pi y/L_y) B_0 d_{i,0}$ . In the Harris equilibrium, the current resulting from the magnetic field configuration is distributed among electrons and ions according to  $u_{z,i}/u_{z,e} = T_i/T_e$ .

The ten moment gradient simulation shown in Fig. 1 has an x-point profile comparable to existing particle-in-cell simulations with large system sizes. The electron outflow jet near the x-point is visible in the right plot in dark blue. Its structure matches the kinetic results shown in Fig. 2 of Nakamura *et al.* (2018b), including the in- and outflow regions along the separatrix boundary. Nakamura *et al.* (2018a) modelled a reconnection event detected by MMS where the outflow jet is similar. A difference between kinetic and ten moment fluid models is that the onset of reconnection takes significantly longer in fluid simulations (Wang *et al.* 2015; Allmann-Rahn *et al.* 2018), and this is also evident here: reconnection peaks around  $t = 56 \Omega_i^{-1}$  whereas in Nakamura *et al.* (2018b) it peaks around  $t = 30 \Omega_i^{-1}$  although there the initial current sheet thickness is larger, which corresponds to a longer onset. This is not a particularly important aspect as Harris sheet reconnection ignores current sheet formation anyway, but it must be considered in three-dimensional simulations. After reconnection, a secondary island evolves at the x-point location. If perturbations are applied to break symmetry, this island is ejected, but in the perfectly symmetric case shown here, the island stays in the middle of the domain and two new x-points are created. When the current sheet enlarges in  $x$ -direction, at later times secondary islands also evolve in kinetic simulations with zero guide field (Karimabadi *et al.* 2007; Klimas *et al.* 2008), but more often when a guide field is present (Drake *et al.* 2006). Ion-scale islands, also referred to as flux transfer events, have been observed in magnetosphere (Hasegawa *et al.* 2016; Hwang *et al.* 2016). Nevertheless, the ten moment gradient model seems to be more susceptible to formation of secondary islands.

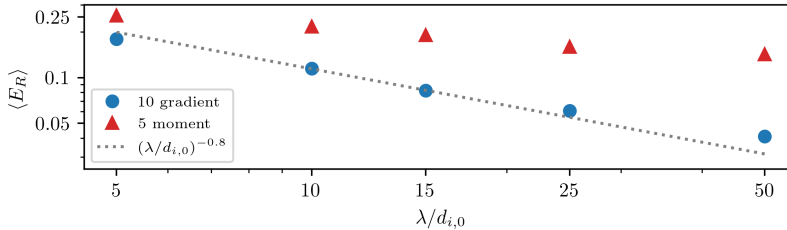


Figure 2: Scaling of average reconnection rate with system size in island coalescence reconnection: ten moment gradient and five moment simulations.

#### 4.2. Island Coalescence

Reconnection studies are often initialised with a perturbed current sheet as described in the previous section. This approach results in reconnection rates and an x-point structure comparable to reconnection events in the magnetosphere. The procedure of reconnection onset, however, differs from that in nature since the formation of the current sheet is not considered. A model that can be applied to the magnetosphere should also be able to capture the physics of current sheet formation appropriately. This can be tested using the island coalescence reconnection setup where kinetic simulations showed lower reconnection rate for larger system sizes (Stanier *et al.* 2015), and the ten-moment fluid model with the gradient closure can reproduce the reconnection rate scaling (Allmann-Rahn *et al.* 2018). The correct time development of reconnection is particularly important for the interplay with current sheet instabilities like the LHDI. In order to see if the kinetic results can be reproduced using the parameters chosen here for Harris sheet reconnection and the lower-hybrid drift instability, we perform island coalescence simulations for different system sizes with  $\chi = 3$  in Eq. (3.4).

The initial geometry is defined by density  $n = n_0(1 - \epsilon^2)/(\cosh(y/\lambda) + \epsilon \cos(x/\lambda))^2 + n_b$  and magnetic potential  $A_z = -\lambda B_0 \ln(\cosh(y/\lambda) + \epsilon \cos(x/\lambda))$  with a system size of  $L_x \times L_y = (2\pi\lambda \times 4\pi\lambda) d_{i,0}$ . For a more detailed description of the setup see Allmann-Rahn *et al.* (2018) (also Stanier *et al.* (2015), Ng *et al.* (2015)). Reconnection rate is evaluated using the magnetic flux, which is the integral over  $B_x$  from the O- to the X-point  $\Psi = \int_O^X B_x dy$  and is normalised over  $B'$ , the maximum of the magnetic field's absolute value at  $x = 0$  and time  $t = 0$ . With  $v'_A = B'/\sqrt{\mu_0 n_0 m_i}$ , the normalised reconnection rate is  $E_R = \frac{\partial \Psi}{\partial t} / (B' v'_A)$ .

In Fig. 2 the average reconnection rate is shown depending on the parameter  $\lambda$  which determines the system size. The dotted line represents the scaling of  $\langle E_R \rangle$  with  $\lambda$  found by Stanier *et al.* (2015) in kinetic particle-in-cell simulations up to  $\lambda = 25 d_{i,0}$ , and the ten moment gradient model comes close to  $\langle E_R \rangle \propto (\lambda/d_{i,0})^{-0.8}$ . Slightly better agreement can be achieved by tuning  $\chi$  and  $k_{s,0}$ , but it is important that the closure works fine with the same parameters in different configurations – and that seems to be the case for  $\chi = 3$  and  $k_{s,0} = 1/d_{s,0}$ . In addition to the ten moment gradient results, we show performance of the five moment model, which is able to capture the lower-hybrid drift instability (cf. Sec. 5) and was not considered in previous studies of island coalescence. The drop of reconnection rate is much smaller and the scaling with system size is only somewhat stronger than that of Hall-MHD in Stanier *et al.* (2015). The ten-moment model using the isotropisation closure or a non-local closure outperform the five moment model, although they do not reach the scaling of the kinetic and ten-moment gradient models (Ng *et al.* 2017; Allmann-Rahn *et al.* 2018).



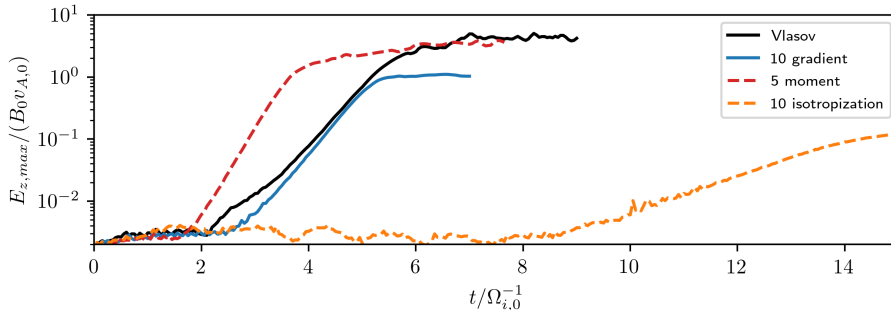


Figure 3: Time development of the supremum norm of  $E_z$  in LHDI simulations ( $m_i/m_e = 100$ ).

### 5. Lower-Hybrid Drift Instability (LHDI)

When magnetic reconnection is simulated in two dimensions, the assumed approximation is that the plasma is homogeneous along the out-of-plane dimension. Thin current sheets, as they are present in reconnection, are often susceptible to instabilities though and these can cause highly turbulent features in the out-of-plane dimension. The initial setup for a two-dimensional analysis of various current sheet instabilities can again be a Harris sheet equilibrium. The connection to the two-dimensional reconnection setup is that instead of the  $x$ - $y$ -plane, now the  $y$ - $z$ -plane is simulated for one fixed point in  $x$ -direction. So the initial configuration is again  $n(y) = n_0 \text{sech}^2(y/\lambda) + n_b$ ,  $B_x(y) = B_0 \tanh(y/\lambda)$ ,  $n_0 k_B (T_e + T_i) = B_0^2/(2\mu_0)$  and  $c = 30 v_{A,0}$ . For the velocity profiles it follows that  $u_{z,s} = 2T_{s,0}B_0 \text{sech}^2(y/\lambda)/(q_s n_s \lambda \mu_0)$ . The instabilities are initiated by adding perturbations which can either be random noise or explicit modes that are supposed to be examined. In PIC simulations, the particle noise also excites instabilities and when single precision calculations are used (especially combined with the FDTD method) even the noise from machine precision drives instabilities. Therefore we utilise double precision calculations in all cases and explicitly initialise perturbations in order to avoid unphysical results. For the LHDI simulations in this section, linearly distributed random noise is added to the initial  $B_x$  with a magnitude of  $10^{-4} B_0$ .

There are four important aspects to consider when studying the LHDI: the growth rate, the duration of onset, the saturation and the potential excitation of secondary instabilities. These characteristics are most influenced by current sheet thickness, background density and ion-electron temperature ratio. Generally, the growth rate is higher for thin current sheets, low background density and high  $T_i/T_e$ . For studying the LHDI we choose parameters as in Ng *et al.* (2019) so that there is the possibility of comparing the results. The parameters are: half-thickness of the current sheet  $\lambda = \rho_{i,0}$ , background density  $n_b = 0.001 n_0$  and temperature ratio  $T_{0,i}/T_{0,e} = 10$ , where  $\rho_{i,0} = \sqrt{k_B T_{i,0}/m_i}/\Omega_{i,0}$  is the ion gyroradius. These are suitable conditions for a fast development of the LHDI. Ng *et al.* (2019) used a mass ratio of  $m_i/m_e = 36$  which is interesting for magnetosphere modelling where reduced mass ratios are common. Nevertheless, it is necessary to consider more realistic mass ratios, both for obtaining physically relevant results and for comparing numerical models. In order to analyse the influence of mass ratio, we perform simulations using different electron masses. The simulated domain is of size  $L_y \times L_z = (6.8 \times 3.4)\rho_{i,0} = (4.6 \times 2.3)d_{i,0}$  with a spatial resolution of  $512 \times 256$  for  $m_i/m_e \leq 100$  and  $1024 \times 512$  for higher mass ratios. In the Vlasov simulations, the extent of velocity space is  $\pm 8v_{t,s}$  resolved by 2.1 cells per  $v_{t,e}$ . In the  $m_i/m_e = 250$  case,



for example, electron velocity space goes from  $-27v_{A,0}$  to  $27v_{A,0}$  and ion velocity space from  $-5v_{A,0}$  to  $5v_{A,0}$  with a total resolution of  $1024 \times 512 \times 114^2$  cells.

Growth rate, onset duration and the mode number that develops are shown in Fig. 4 for the Vlasov model, the ten moment model using the gradient closure, the five moment model and the ten moment model using the isotropisation closure in Wang *et al.* (2015). Growth rate  $\kappa$  is determined via a fit in the phase where  $\|E_z\|_\infty \propto \exp(\kappa t)$  and we define the instability's onset duration as the time until  $\|E_z\|_\infty \geq 0.02 B_0 v_{A,0}$  which was the value where exponential growth started in the simulations.

The growth rate agrees reasonably well between the kinetic Vlasov model and the ten moment gradient model. For the  $m_i/m_e = 100$  case, time development of the electric field is shown in Fig. 3 where the curves' slopes correspond to the growth rates. The growth rates are  $2.2 \Omega_{i,0}$  and  $2.4 \Omega_{i,0}$  for the Vlasov and ten moment gradient models, respectively, whereas growth rate is higher in the five moment model ( $3.2 \Omega_{i,0}$ ) and significantly lower in the ten moment isotropisation model ( $0.67 \Omega_{i,0}$ ). The latter approximates the divergence of heat flux as  $\nabla \cdot \mathbf{Q}_s = k_{s,0} v_{t,s} (P_s - p_s \text{id})$  and we choose  $k_{s,0} = 1/d_{s,0}$  for the free parameter which was used in reconnection studies. When  $k_{s,0} \rightarrow \infty$ , the isotropisation closure approaches the five moment limit (isotropy) and the growth rate increases accordingly. In this case, however, reconnection cannot be modelled well. Vlasov simulations with high mass ratios are not feasible, but we performed ten moment gradient simulations with realistic mass ratio, and the growth rate goes up to  $4 \Omega_{i,0}$ . This should be considered when interpreting magnetosphere simulations where severely reduced mass ratios such as  $m_i/m_e = 25$  are employed.

The onset duration is, for Harris sheet reconnection simulations, as relevant as the growth rate since the influence of the LHDI at a certain time results from the combination of both. It is important to note that the onset duration depends heavily on the magnitude of the initial perturbation. But when the perturbation is fixed, the duration until exponential growth starts can be examined for the various models. In Fig. 5 the structure and magnitude of the electric field at a certain time is shown, which gives an impression of the combined effect of onset duration and growth rate. The difference between the ten moment gradient model and the Vlasov model is small and the slightly higher E-field value in the Vlasov case results from the earlier onset. The five moment model is already in a state where the fastest growing mode has saturated and secondary modes are excited.

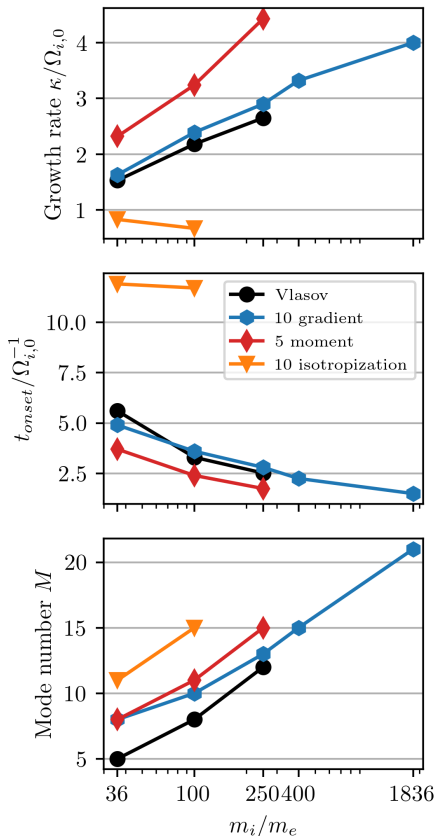


Figure 4: Scaling of LHDI characteristics with mass ratio for different models. Growth rate of the instability (upper), onset duration (middle) and number of modes (lower).

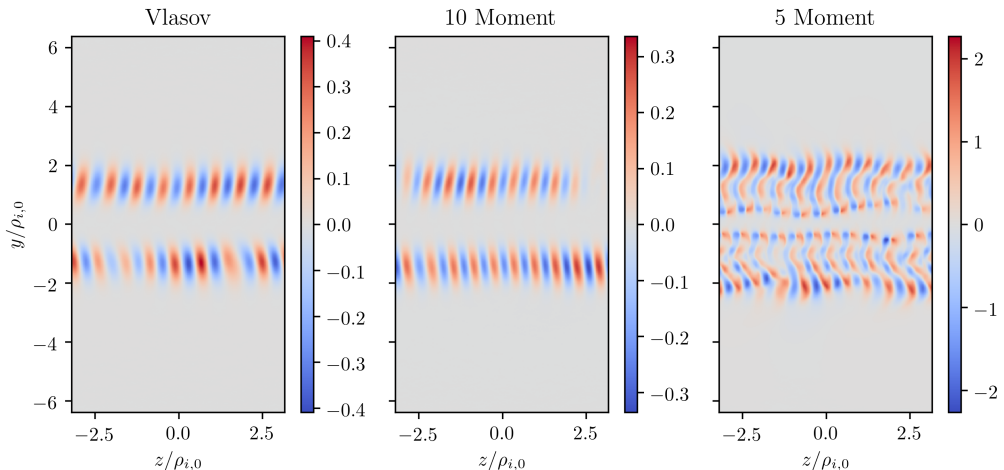


Figure 5:  $E_z / (B_0 v_{A,0})$  in simulations of the LHD at  $t = 4.75 \Omega_{i,0}^{-1}$  for the Vlasov model, the ten moment gradient model and the five moment model ( $m_i/m_e = 100$ ).

This rapid development can be attributed more to the very fast onset than to the higher growth rate. The five moment results are in contrast to the findings of Ng *et al.* (2019) who reported a much too slow LHD growth using this model. They agree, however, with a study by TenBarge *et al.* (2019) who modelled an MMS reconnection event and found the five moment model to be not well-suited due to explosive growth of the LHD. Our findings are also consistent with the  $k_{s,0} \rightarrow \infty$  limit of the ten moment isotropisation closure. The onset time in the ten moment isotropisation model using normal parameters is very late, decreases with mass ratio, and for  $m_i/m_e = 250$  no instability grows at all during the simulated time span.

The mode number shown in Fig. 4 is defined as the  $M = k_z \rho_{i,0}$  that develops out of random noise in the respective simulation and thus corresponds to the fastest growing mode (or one of the fastest, if growth rates are very close for several modes). The mode numbers do not agree between the Vlasov and fluid models for low mass ratios. While the number of modes itself is of little relevance for reconnection, it is crucial to always look at the respectively fastest growing modes when comparing different models. Ng *et al.* (2019) explicitly initialised the  $M = 8$  mode which is the fastest mode for the fluid models but in the  $m_i/m_e = 36$  case a rather slow mode in the Vlasov model (we obtain a growth rate of  $1.1 \Omega_{i,0}$  for the  $M = 8$  mode in agreement with Ng *et al.* (2019)). Therefore, only looking at a single mode is not an appropriate method of measuring the capability of fluid models to reproduce the kinetic LHD. Towards more realistic electron masses, mode numbers increase as expected, and they are close for the Vlasov model and the ten moment gradient model at  $m_i/m_e = 250$ .

There is a second reason why random noise is the preferable way of initialising the LHD. As visible in Fig. 5, an  $M = 1$  or  $M = 2$  modulation of the LHD is present which does not develop from the initialisation of a single Fourier mode. This modulation with a longer wavelength than that of the LHD exists in both Vlasov and fluid models at all simulated mass ratios. It may be attributed to an ion-ion kink instability, the drift kink instability with non-linearities or a Kelvin-Helmholtz type instability (Lapenta *et al.* 2003). If a Fourier mode is initialised, the LHD saturates and leaves the current sheet intact. When the interplay with the kink-type instability is considered, however, at later

times the kinking leads to a disruption of the current sheet and highly turbulent features which can affect reconnection considerably as discussed in Sec. 6. From Fig. 3 it becomes apparent that the LHDI saturates at a lower level in the ten moment gradient model compared to the kinetic results. Typically, peaks in the current density are lower for the ten moment fluid model with the closures used here (Juno *et al.* 2018; Allmann-Rahn *et al.* 2018), and we confirmed that  $j_y$ , which is related to the field strength, has a higher magnitude in the Vlasov simulations. However, the saturation level of the first appearing LHDI mode is less important as the electric field’s magnitude becomes larger at later times due to kinking and turbulence. We want to mention that the electromagnetic LHDI is also supported by the fluid models but did not play a role in the three-dimensional reconnection simulation, so we will not analyze it here. The development of the electrostatic LHDI and kink/Kelvin-Helmholtz instabilities with GEM-like background density and temperature ratio will be discussed in the following section.

The mass ratio dependence in the LHDI simulations supports our choice of  $k_{s,0} = 1/d_{s,0}$  in the gradient closure. More heat flux due to the closure leads to increased LHDI growth rates and earlier onset. Since  $d_{s,0} \propto \sqrt{m_s}$ , the higher  $k_{s,0}$  compensates the increased heat flux caused by  $v_{t,s}$  in the closure at small electron masses and prevents the electrons from being thermalized. If  $k_{s,0}$  is chosen to be independent of mass, the LHDI grows too fast at high mass ratios, whereas with  $k_{s,0} = 1/d_{s,0}$  there is good agreement between kinetic and ten moment gradient results.

## 6. Three-Dimensional Reconnection

In order to examine the effect of the LHDI on reconnection, we study the interplay of the two in a three-dimensional setup that is identical to the one of the Harris sheet reconnection simulation in Sec. 4.1 – except for the additional dimension and a tiny initial perturbation of electron density. The domain now has the size  $L_x \times L_y \times L_z = (32\pi \times 8\pi \times 2\pi)d_{i,0} \approx (100 \times 25 \times 6)d_{i,0}$  with a resolution of  $2400 \times 600 \times 150$  cells and periodic boundary conditions in  $z$ -direction. Linearly distributed random noise is added to the initial electron density with a maximum magnitude of  $\delta n_e = 10^{-8}n_0$  so that instabilities like the LHDI can develop. The perturbation’s magnitude influences the LHDI’s onset duration and therefore has great impact on the effect of the LHDI, as will be discussed later. Using a small random perturbation of electron density, we give current sheet instabilities maximum freedom in their development.

Contour renderings of the current density  $j_z$  are given in Fig. 6 after the reconnection current sheet has formed and at a later stage when turbulence dominates. The upper plot shows the same time as Fig. 1 for the two-dimensional case and similar features are visible with a slightly smaller  $x$ -line current sheet in the three-dimensional simulation. Fluctuations in the third dimension are moderate in the electron diffusion region but strong in the outflow where the combination of the lower-hybrid drift and kink/Kelvin-Helmholtz instabilities has disrupted the current sheet. The LHDI mode affects the current density and can be seen in the contours at  $t = 65 \Omega_{i,0}^{-1}$  left and right of the  $x$ -line. Around  $t = 68 \Omega_{i,0}^{-1}$  a secondary island (plasmoid) forms and is ejected in the negative  $x$ -direction. Later, the electron diffusion region becomes more turbulent and the  $x$ -line current sheet broadens, as is visible in the lower panel.

The reconnection rate is shown in Fig. 7 (top) for both 2D and 3D, evaluated by averaging the value of  $E_z$  at the  $x$ -line over  $z$ , the  $x$ -line being the location where  $u_{z,e}$  has a maximum. What stands out is that the reconnection rate falls rapidly after  $t = 66 \Omega_{i,0}^{-1}$  in both cases corresponding to the formation of a secondary island. Since the island

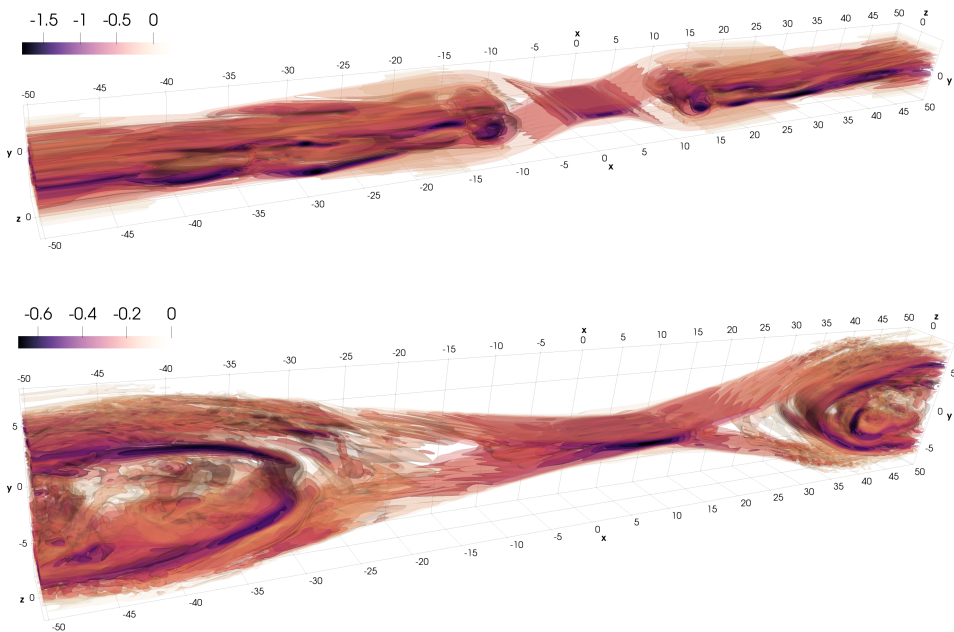


Figure 6: Contour plots of  $j_z/(n_0 v_{A,0})$  from the three-dimensional reconnection simulation at times  $t = 65 \Omega_{i,0}^{-1}$  (upper) and  $t = 95 \Omega_{i,0}^{-1}$  (lower).

is not ejected in the two-dimensional simulation with perfect symmetry, reconnection rate is only plotted as long as there is a single defined x-line. The earlier start of fast reconnection in three dimensions can likely be attributed to current sheet thinning and electron heating caused by the LHDI. After fast reconnection has started, the increased electron temperature in the electron diffusion region leads to a decay of the LHDI which may be the reason for the temporary drop of the reconnection rate at  $t = 48 \Omega_{i,0}^{-1}$ . The development of instabilities at the x-line is demonstrated in Fig. 8 at three exemplary points in time. The LHDI (left) is weaker and arises later at the x-line than in the rest of the current sheet and when fast reconnection has started it decays and leaves moderate turbulence behind (middle) caused by secondary modes. In the later stage, a different instability emerges (right) which has common features with the current sheet shear instability (CSSI) shown in Fig. 3 of [Fujimoto & Sydora \(2017\)](#) concerning wave length,  $y$ -extent and magnitude. To confirm whether the instability in our simulation is indeed the CSSI will be left for future work as it is not the primary subject of this study. However, the structure of the electric field at the x-line does agree with the kinetic PIC simulation of three-dimensional reconnection in [Fujimoto & Sydora \(2017\)](#) although there the turbulence is much stronger around the x-line. In contrast, [Nakamura \*et al.\* \(2018a\)](#) found negligible three-dimensionality in the electron diffusion region. This is not necessarily a contradiction and is likely caused by the different background densities which were  $0.044 n_0$  in the former and  $0.3 n_0$  in the latter study attended by respectively fast or slow growth of the LHDI. The low temperature ratio of  $T_i/T_e = 3$  in [Nakamura \*et al.\* \(2018a\)](#) may have further slowed down the LHDI development. Our setup with  $n_b = 0.2 n_0$  and  $T_i/T_e = 5$  lies between the two which is also evident in the amount of turbulence present.

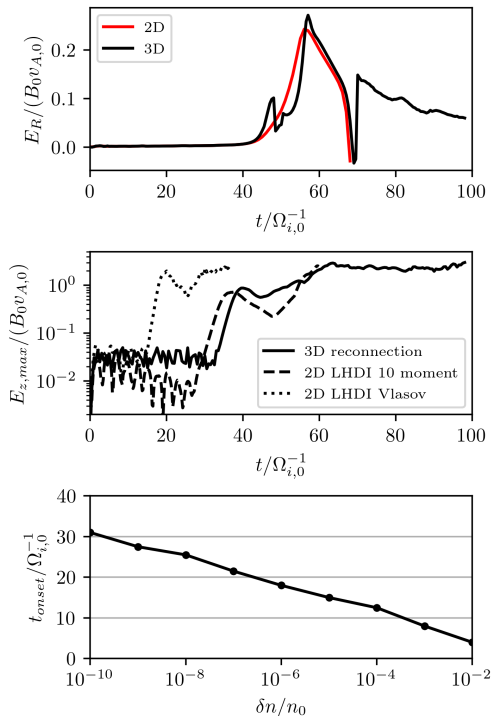


Figure 7: Reconnection rate (upper), supremum norm of  $E_z$  in three-dimensional reconnection compared to two-dimensional LHDI (middle) and LHDI onset duration depending on initial perturbation (lower).

development is again comparable but onset time is much earlier and growth rate is also higher ( $1.08 \Omega_{i,0}$  compared to  $0.61 \Omega_{i,0}$  in the fluid model). The faster onset of the LHDI using the kinetic model in this setup is consistent with the faster onset of reconnection so that in the end the effect of the LHDI in ten moment gradient simulations resembles the effect in kinetic simulations.

In particle-in-cell simulations numerical noise is unavoidable, present at all times, and its magnitude depends on the amount of particles used. In contrast, continuum models, such as the fluid model used here, offer complete control over the perturbation level and thus the onset duration of instabilities. The LHDI's onset time does indeed depend heavily on the perturbation. In order to demonstrate this, we apply initial perturbations of different magnitudes  $\delta n$  to electron and ion density in the current sheet setup used for the Harris sheet reconnection simulations, and measure the onset duration (time until  $\|E_z\|_\infty \geq 0.04 B_0 v_{A,0}$ ). The results are shown in Fig. 7 (lower). The onset duration has an approximately logarithmic dependence  $t_{onset} \sim \log(\delta n / n_0)$  in this setup using a resolution as in the three-dimensional simulation. There is a wide range between  $t_{onset} = 30 \Omega_{i,0}^{-1}$  when  $\delta n = 10^{-10} n_0$  and  $t_{onset} = 4 \Omega_{i,0}^{-1}$  when  $\delta n = 10^{-2} n_0$  and the time development is substantially different even when comparing for example an initialisation using  $\delta n = 10^{-6} n_0$  and one using  $\delta n = 10^{-4} n_0$ . There is also competition between the LHDI onset and the reconnection onset, which can be influenced by the magnitude of perturbation in the magnetic flux  $\psi$ . Thus, depending on the initial perturbation one can

There are two major differences between kinetic particle-in-cell simulations and fluid simulations, namely the longer reconnection onset of the fluid model and the numerical noise of the PIC model. Both will be discussed, starting with the reconnection onset duration. While it is of no particular interest in two-dimensional reconnection, a longer onset duration in three dimensions gives instabilities more time to affect and potentially disrupt the current sheet before reconnection due to the initially applied  $B$ -field perturbation takes place. We compared the LHDI development in two-dimensional Vlasov and ten moment gradient simulations with the one within three-dimensional reconnection using the same initial conditions for the current sheet. The electric field's evolution is given in Fig. 7 (middle). Comparing the ten moment simulation of pure LHDI with the reconnection simulation, the development is very similar indicating that the LHDI is the main source of fluctuations in  $E_z$  as expected. Its onset is slightly later within reconnection because of the broader current sheet that develops in the course of the reconnection process.

Looking at the Vlasov simulation, the

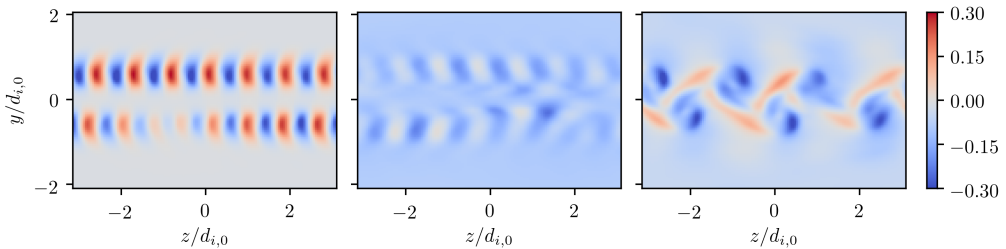


Figure 8: Instabilities at the x-line in 3D reconnection. Shown are y-z-slices of  $E_z/(B_0 v_{A,0})$  at times  $t = 42 \Omega_{i,0}^{-1}$  (left),  $t = 54 \Omega_{i,0}^{-1}$  (middle) and  $t = 98.5 \Omega_{i,0}^{-1}$  (right).

get highly turbulent reconnection with x-lines due to current sheet instabilities or weak effect of instabilities and a reconnection that is essentially two-dimensional. A prediction of the influence of instabilities in magnetospheric reconnection events would therefore need accurate information on perturbation levels. This is also a challenge for particle-in-cell codes where control over numerical noise is limited. Generally, a Harris sheet setup does not realistically describe the process of current sheet formation and the time until fast reconnection starts, which must be considered when interpreting results from simulations that assume an already formed current sheet. However, three-dimensional Harris sheet simulations provides valuable insight in the possible scenarios concerning turbulence in magnetospheric reconnection.

## 7. Summary and Future Work

The ten moment fluid model with a closure based on pressure gradients can appropriately represent magnetic reconnection and the lower-hybrid drift instability (LHDI), making it a suitable candidate for magnetospheric modelling. The same parameters in the closure are viable for a broad range of plasma configurations in the collisionless regime. Compared to kinetic particle-in-cell simulations, computational cost is lower and there is explicit control over perturbations. We found that the LHDI combined with a kink-type instability can cause significant turbulence and affect reconnection depending on plasma parameters such as the initial perturbation and the background density. In the three-dimensional reconnection simulation reconnection onset was faster than in two dimensions and the current sheet broadened in the later stages. Strong turbulence in the outflow and moderate turbulence in the electron diffusion region was observed to develop.

Future work on the heat flux closure may take into account the direction imposed by the magnetic field, which has not been considered at this point. The formation of magnetic islands in connection with the ten moment gradient model needs further investigation. The LHDI has been the subject of many in-depth studies, but a direct comparison of particle-in-cell and continuum models can shed more light on the role of perturbations and numerical noise. This paper focused on the LHDI which is the first instability to arise, and the effect of instabilities at later times such as the current sheet shear instability will need to be addressed in the future. The process of reconnection onset and the connection with instabilities is not well understood and three-dimensional simulations of reconnection that take current sheet formation into account may provide new insights in this direction.



## Acknowledgements

We gratefully acknowledge the Gauss Centre for Supercomputing e.V. ([www.gauss-centre.eu](http://www.gauss-centre.eu)) for funding this project by providing computing time through the John von Neumann Institute for Computing (NIC) on the GCS Supercomputer JUWELS at Jlich Supercomputing Centre (JSC). Computations were conducted on JUWELS ([Jülich Supercomputing Centre 2019](#)) and on the DaVinci cluster at TP1 Plasma Research Department.

## REFERENCES

- ALLMANN-RAHN, F., TROST, T. & GRAUER, R. 2018 Temperature gradient driven heat flux closure in fluid simulations of collisionless reconnection. *Journal of Plasma Physics* **84** (3), 905840307.
- BIRN, J., DRAKE, J. F., SHAY, M. A., ROGERS, B. N., DENTON, R. E., HESSE, M., KUZNETSOVA, M., MA, Z. W., BHATTACHARJEE, A., OTTO, A. & PRITCHETT, P. L. 2001 Geospace environmental modeling (gem) magnetic reconnection challenge. *Journal of Geophysical Research: Space Physics* **106** (A3), 3715–3719.
- BRAGINSKII, S. I. 1965 Transport processes in a plasma. *Reviews of Plasma Physics* **1**, 205.
- DAUGHTON, W. 2003 Electromagnetic properties of the lower-hybrid drift instability in a thin current sheet. *Physics of Plasmas* **10** (8), 3103–3119.
- DONG, C., WANG, L., HAKIM, A., BHATTACHARJEE, A., SLAVIN, J. A., DIBRACCIO, G. A. & GERMASCHESKI, K. 2019 Global ten-moment multifluid simulations of the solar wind interaction with mercury: From the planetary conducting core to the dynamic magnetosphere. *Geophysical Research Letters* **46** (21), 11584–11596.
- DRAKE, J. F., SWISDAK, M., SCHOEFFLER, K. M., ROGERS, B. N. & KOBAYASHI, S. 2006 Formation of secondary islands during magnetic reconnection. *Geophysical Research Letters* **33** (13).
- EGEDAL, J., LE, A. & DAUGHTON, W. 2013 A review of pressure anisotropy caused by electron trapping in collisionless plasma, and its implications for magnetic reconnection. *Phys. Plasmas* **20**, 061201.
- EGEDAL, J., NG, J., LE, A., DAUGHTON, W., WETHERTON, B., DORELLI, J., GERSHMAN, D. & RAGER, A. 2019 Pressure tensor elements breaking the frozen-in law during reconnection in earth’s magnetotail. *Phys. Rev. Lett.* **123**, 225101.
- FILBET, F., SONNENDRCKER, E. & BERTRAND, P. 2001 Conservative numerical schemes for the vlasov equation. *Journal of Computational Physics* **172** (1), 166 – 187.
- FUJIMOTO, K. & SYDORA, R. D. 2012 Plasmoid-induced turbulence in collisionless magnetic reconnection. *Phys. Rev. Lett.* **109**, 265004.
- FUJIMOTO, K. & SYDORA, R. D. 2017 Linear theory of the current sheet shear instability. *Journal of Geophysical Research: Space Physics* **122** (5), 5418–5430.
- HAMMETT, G. W., DORLAND, W. & PERKINS, F. W. 1992 Fluid models of phase mixing, landau damping, and nonlinear gyrokinetic dynamics. *Physics of Fluids B* **4** (7), 2052–2061.
- HAMMETT, G. W. & PERKINS, F. W. 1990 Fluid moment models for landau damping with application to the ion-temperature-gradient instability. *Phys. Rev. Lett.* **64**, 3019–3022.
- HARRIS, E. G. 1962 On a plasma sheath separating regions of oppositely directed magnetic field. *Il Nuovo Cimento (1955-1965)* **23** (1), 115–121.
- HASEGAWA, H., KITAMURA, N., SAITO, Y., NAGAI, T., SHINOHARA, I., YOKOTA, S., POLLOCK, C. J., GILES, B. L., DORELLI, J. C., GERSHMAN, D. J., AVANOV, L. A., KREISLER, S., PATERSON, W. R., CHANDLER, M. O., COFFEY, V., BURCH, J. L., TORBERT, R. B., MOORE, T. E., RUSSELL, C. T., STRANGWAY, R. J., LE, G., OKA, M., PHAN, T. D., LAVRAUD, B., ZENITANI, S. & HESSE, M. 2016 Decay of mesoscale flux transfer events during quasi-continuous spatially extended reconnection at the magnetopause. *Geophysical Research Letters* **43** (10), 4755–4762.
- HESSE, M., WINSKE, D. & KUZNETSOVA, M. M. 1995 Hybrid modeling of collisionless reconnection in two-dimensional current sheets: Simulations. *Journal of Geophysical Research: Space Physics* **100** (A11), 21815–21825.



- HWANG, K.-J., SIBECK, D. G., GILES, B. L., POLLOCK, C. J., GERSHMAN, D., AVANOV, L., PATERSON, W. R., DORELLI, J. C., ERGUN, R. E., RUSSELL, C. T., STRANGEWAY, R. J., MAUK, B., COHEN, I. J., TORBERT, R. B. & BURCH, J. L. 2016 The substructure of a flux transfer event observed by the mms spacecraft. *Geophysical Research Letters* **43** (18), 9434–9443.
- JOHNSON, E. A. & ROSSMANITH, J. A. 2010 Ten-moment two-fluid plasma model agrees well with pic/vlasov in gem problem. *ArXiv e-prints*, arXiv: 1010.0746.
- JÜLICH SUPERCOMPUTING CENTRE 2019 JUWELS: Modular Tier-0/1 Supercomputer at the Jülich Supercomputing Centre. *Journal of large-scale research facilities* **5** (A135).
- JUNO, J., HAKIM, A., TENBARGE, J., SHI, E. & DORLAND, W. 2018 Discontinuous galerkin algorithms for fully kinetic plasmas. *Journal of Computational Physics* **353**, 110 – 147.
- KARIMABADI, H., DAUGHTON, W. & SCUDDER, J. 2007 Multi-scale structure of the electron diffusion region. *Geophysical Research Letters* **34** (13).
- KLIMAS, A., HESSE, M. & ZENITANI, S. 2008 Particle-in-cell simulation of collisionless reconnection with open outflow boundaries. *Physics of Plasmas* **15** (8), 082102.
- KURGANOV, A. & LEVY, D. 2000 A third-order semidiscrete central scheme for conservation laws and convection-diffusion equations. *SIAM Journal on Scientific Computing* **22** (4), 1461–1488.
- LAPENTA, G., BRACKBILL, J. U. & DAUGHTON, W. S. 2003 The unexpected role of the lower hybrid drift instability in magnetic reconnection in three dimensions. *Physics of Plasmas* **10** (5), 1577–1587.
- LE, A., DAUGHTON, W., KARIMABADI, H. & EGEDAL, J. 2016 Hybrid simulations of magnetic reconnection with kinetic ions and fluid electron pressure anisotropy. *Physics of Plasmas* **23** (3), 032114.
- LE, A., EGEDAL, J., DAUGHTON, W., FOX, W. & KATZ, N. 2009 The equations of state for collisionless guide-field reconnection. *Phys. Rev. Lett.* **102**, 085001.
- LE, A., STANIER, A., DAUGHTON, W., NG, J., EGEDAL, J., NYSTROM, W. D. & BIRD, R. 2019 Three-dimensional stability of current sheets supported by electron pressure anisotropy. *Physics of Plasmas* **26** (10), 102114.
- NAKAMURA, T. K. M., GENESTRETI, K. J., LIU, Y.-H., NAKAMURA, R., TEH, W.-L., HASEGAWA, H., DAUGHTON, W., HESSE, M., TORBERT, R. B., BURCH, J. L. & GILES, B. L. 2018a Measurement of the magnetic reconnection rate in the earth’s magnetotail. *Journal of Geophysical Research: Space Physics* **123** (11), 9150–9168.
- NAKAMURA, T. K. M., NAKAMURA, R., VARSANI, A., GENESTRETI, K. J., BAUMJOHANN, W. & LIU, Y.-H. 2018b Remote sensing of the reconnection electric field from in situ multipoint observations of the separatrix boundary. *Geophysical Research Letters* **45** (9), 3829–3837.
- NG, J., HAKIM, A., BHATTACHARJEE, A., STANIER, A. & DAUGHTON, W. 2017 Simulations of anti-parallel reconnection using a nonlocal heat flux closure. *Physics of Plasmas* **24** (8), 082112.
- NG, J., HAKIM, A., JUNO, J. & BHATTACHARJEE, A. 2019 Drift instabilities in thin current sheets using a two-fluid model with pressure tensor effects. *Journal of Geophysical Research: Space Physics* **124** (5), 3331–3346.
- NG, J., HUANG, Y.-M., HAKIM, A., BHATTACHARJEE, A., STANIER, A., DAUGHTON, W., WANG, L. & GERMASCHESKI, K. 2015 The island coalescence problem: Scaling of reconnection in extended fluid models including higher-order moments. *Physics of Plasmas* **22** (11), 112104.
- PASSOT, T. & SULEM, P. L. 2003 Long-alfvén-wave trains in collisionless plasmas. ii. a landau-fluid approach. *Physics of Plasmas* **10** (10), 3906–3913.
- SCHMITZ, H. & GRAUER, R. 2006 Comparison of time splitting and backsubstitution methods for integrating vlasov’s equation with magnetic fields. *Comp. Phys. Comm.* **175**, 86.
- SHARMA, P., HAMMETT, G. W. & QUATAERT, E. 2003 Transition from collisionless to collisional magnetorotational instability. *The Astrophysical Journal* **596**, 1121.
- SHARMA, P., HAMMETT, G. W., QUATAERT, E. & STONE, J. M. 2006 Shearing box simulations of the MRI in a collisionless plasma. *The Astrophysical Journal* **637** (2), 952–967.
- SHU, C.-W. & OSHER, S. 1988 Efficient implementation of essentially non-oscillatory shock-capturing schemes. *Journal of Computational Physics* **77** (2), 439 – 471.

- SNYDER, P. B., HAMMETT, G. W. & DORLAND, W. 1997 Landau fluid models of collisionless magnetohydrodynamics. *Physics of Plasmas* **4** (11), 3974–3985.
- STANIER, A., DAUGHTON, W., CHACÓN, L., KARIMABADI, H., NG, J., HUANG, Y.-M., HAKIM, A. & BHATTACHARJEE, A. 2015 Role of ion kinetic physics in the interaction of magnetic flux ropes. *Phys. Rev. Lett.* **115**, 175004.
- TENBARGE, J. M., NG, J., JUNO, J., WANG, L., HAKIM, A. H. & BHATTACHARJEE, A. 2019 An extended mhd study of the 16 october 2015 mms diffusion region crossing. *Journal of Geophysical Research: Space Physics* **124** (11), 8474–8487.
- WANG, L., GERMASCHEWSKI, K., HAKIM, A., DONG, C., RAEDER, J. & BHATTACHARJEE, A. 2018 Electron physics in 3-d two-fluid 10-moment modeling of ganymede’s magnetosphere. *Journal of Geophysical Research: Space Physics* **123** (4), 2815–2830.
- WANG, L., HAKIM, A. H., BHATTACHARJEE, A. & GERMASCHEWSKI, K. 2015 Comparison of multi-fluid moment models with particle-in-cell simulations of collisionless magnetic reconnection. *Physics of Plasmas* **22** (1), 012108.
- WANG, L., HAKIM, A. H., NG, J., DONG, C. & GERMASCHEWSKI, K. 2020 Exact and locally implicit source term solvers for multifluid-maxwell systems. *Journal of Computational Physics* **415**, 109510.
- YAMADA, M., JI, H., HSU, S., CARTER, T., KULSRUD, R., BRETZ, N., JOBES, F., ONO, Y. & PERKINS, F. 1997 Study of driven magnetic reconnection in a laboratory plasma. *Physics of Plasmas* **4** (5), 1936–1944.